UNIVERSITY OF LEEDS

This is a repository copy of *The fennec automatic weather station (AWS) network: Monitoring the Saharan climate system*.

White Rose Research Online URL for this paper:
http://eprints.whiterose.ac.uk/79055/

Version: Published Version

Article:

eprints@whiterose.ac.uk
https://eprints.whiterose.ac.uk/

The Fennec Automatic Weather Station (AWS) Network: Monitoring the Saharan Climate System

MATTHEW HOBBY,* MATTHEW GASCOYNE,* JOHN H. MARSHAM,[+] MARK BART,*
CHRISTOPHER ALLEN,[#] SEBASTIAN ENGELSTAEDTER,[#] DIEH MOHAMED FADEL,[@]
ABDOULAYE GANDEGA,[@] RICHARD LANE,* JAMES B. MCQUAID,* BOUZIANE OUCHENE,[&]
ABDELKADER OULADICHIR,[&] DOUGLAS J. PARKER,* PHIL ROSENBERG,*
MOHAMMED SALAH FERROUDJ,[&] AZZEDINE SACI,[&] FOUAD SEDDIK,[&] MARTIN TODD,**
DAN WALKER,[+] AND RICHARD WASHINGTON[#]

* University of Leeds, Leeds, United Kingdom
[+] National Centre for Atmospheric Science, University of Leeds, Leeds, United Kingdom
[#] University of Oxford, Oxford, United Kingdom
[@] Office National de la Meteorologie, Nouakchott, Mauritania
[&] Office National de la Meteorologie, Algiers, Algeria
** University of Sussex, Brighton, United Kingdom

ABSTRACT

The Fennec automatic weather station (AWS) network consists of eight stations installed across the Sahara, with four in remote locations in the central desert, where no previous meteorological observations have existed. The AWS measures temperature, humidity, pressure, wind speed, wind direction, shortwave and longwave radiation (upwelling and downwelling), ground heat flux, and ground temperature. Data are recorded every 3 min 20 s, that is, at 3 times the temporal resolution of the World Meteorological Organization's standard 10-min reporting for winds and wind gusts. Variations in wind speeds on shorter time scales are recorded through the use of second- and third-order moments of 1-Hz data. Using the Iridium Router-Based Unrestricted Digital Internetworking Connectivity Solutions (RUDICS) service, data are transmitted in near–real time (1-h lag) to the United Kingdom, where calibrations are applied and data are uploaded to the Global Telecommunications System (GTS), for assimilation into forecast models.

This paper describes the instrumentation used and the data available from the network. Particular focus is given to the engineering applied to the task of making measurements in this remote region and challenging climate. The communications protocol developed to operate over the Iridium RUDICS satellite service is described. Transmitting the second moment of the wind speed distribution is shown to improve estimates of the dust-generating potential of observed winds, especially for winds close to the threshold speed for dust emission of the wind speed distribution. Sources of error are discussed and some preliminary results are presented, demonstrating the system's potential to record key features of this region.

1. Introduction

The Sahara is the world's largest desert and exhibits a number of climatic extremes—temperature, aridity, and airborne dust loadings, in particular. It is the world's greatest annual source of airborne mineral dust (Prospero et al. 2002; Washington et al. 2003). In recent years it has also been realized that the Saharan heat low (Lavaysse et al. 2009) has a significant influence on the regional climate of North Africa and beyond, influencing the intraseasonal variability and onset of the West African monsoon (Parker et al. 2005b; Sultan et al. 2003; Sultan and Janicot 2003) and the climatic circulation of a much wider region, including western Europe (Rodwell and Jung 2008). At the same time, there are substantial discrepancies between the climatology of models for this region. There have been a handful of research measurements made in this region in recent years (Parker et al. 2005a; Cuesta et al. 2008; Messager et al.

2010; Haywood et al. 2011), but apart from operational observing stations on the margins of the desert, including the observing station at Tamanrasset (WMO station 60680), which is at high altitude, there have been few reliable observations of the Saharan heat low with which to evaluate these models. This lack of data from a key driver of the regional climate motivated the observational program of the Fennec project and dictated that a key goal of Fennec would be to obtain high-quality measurements from the center of the Sahara for model evaluation. In situ measurements are vital because of the need to quantify the Saharan heat low. Furthermore, local wind effects and turbulence drive dust uplift and play a part in cloud growth. Neither of these important processes can be measured using satelliteborne remote sensing.

The reason such measurements have not been made before has to do with the logistical challenge of deploying and operating instruments in this remote area and the technological challenges posed by the climatic extremes of the central Sahara. These technological challenges relate to the extreme heat, airborne sand and dust, remoteness from grid power and habitation, problems of data retrieval, and the need for robustness of instruments in the face of the climatic conditions. In particular, blowing sand causes significant abrasion of instruments, while the deposition of dust causes a number of problems including the abrasion of moving parts (e.g., fans) and the obscuring of solar panels and radiation sensors.

The objectives of this paper are to describe the novel instrument set that has recently been deployed in this unique environment, with some of the technological solutions that have gone into its deployment, including some examples of the high-quality data obtained and its potential uses. We hope that this information is valuable, both to those scientists exploiting the dataset in future years and to others conducting research in similarly harsh environments.

Section 3 provides an overview of the automatic weather station (AWS) design, which integrates a number of instruments and sensors with data logging and communication. Section 4 describes the individual sensor specification, which was determined by the science requirements for Saharan weather and climate science. Section 5 details specific technological solutions, and section 6 outlines the quality control processes and the expected sources of error in the measurements made.

In section 7, we illustrate the potential capability of the observing network with a focus on the use of winds for understanding dust uplift processes. The processes illustrated in section 7 will be the subjects of future detailed studies and are provided here so as to provide context to the measurements described. The final section provides a summary of development work described herein.

2. AWS scientific requirements

The Fennec project aimed to study a wide variety of phenomena in the region, involving a wide range of time scales requiring a broad choice of sensors. These requirements are summarized with relation to the phenomena.

On the synoptic scale, there is a need to measure the evolution of the Saharan heat low, from day to day and as it evolves over the season. For this reason, pressure measurements at accuracy of 0.5 hPa are required. Given that the heat low is driven by the daily temperature evolution, which in turn is controlled by the column irradiative budget, irradiative and ground heat flux measurements are needed, along with surface values of temperatures and humidity. Triaxis sonic anemometers, from which sensible heat fluxes could be computed, are deemed to be insufficiently robust to operate on the AWSs. Additionally, calculating heat flux values is prohibitively data intensive, requiring considerable local processing, large amounts of data storage, or data transmission. However, since the latent heat flux is expected to be small in the Saharan region, due to the low humidity, the sensible heat flux can be estimated as the residual between the net radiation and the ground heat flux.

To allow AWS data to be assimilated into operational weather models, as well as to allow data retrieval from remote locations, data are required to be transmitted hourly by satellite to Leeds in the United Kingdom, where calibrations are applied and the results transmitted to the World Meteorological Organization Global Telecommunications System (WMO GTS) and made available to collaborating national meteorological services in North Africa (the Office National de Meteorologie d'Algerie and the Office National de Meteorologie de Mauritanie).

For the sampling of events such as dust-laden gravity currents (known locally as haboobs), which are thought to control a substantial part of dust uplift as well as influence the regional thermodynamic budget (Peyrille and Lafore 2007; Flamant et al. 2007; Marsham et al. 2008b, 2011a,b), and boundary layer turbulence (e.g., Koch and Renno 2005; Marsham et al. 2008a), higher-frequency pressure, winds, thermodynamic, and flux observations are needed. The AWS's 200-s time sampling, with the collection of wind statistics within each 200-s sample, was therefore a compromise between desired high frequency and satellite data transmission costs [200 s is one-third of the standard WMO 10-min sampling for winds and wind gusts (WMO 2008)].

The scientific requirement outline was used to select the sensors, as described in section 4. Each sensor was
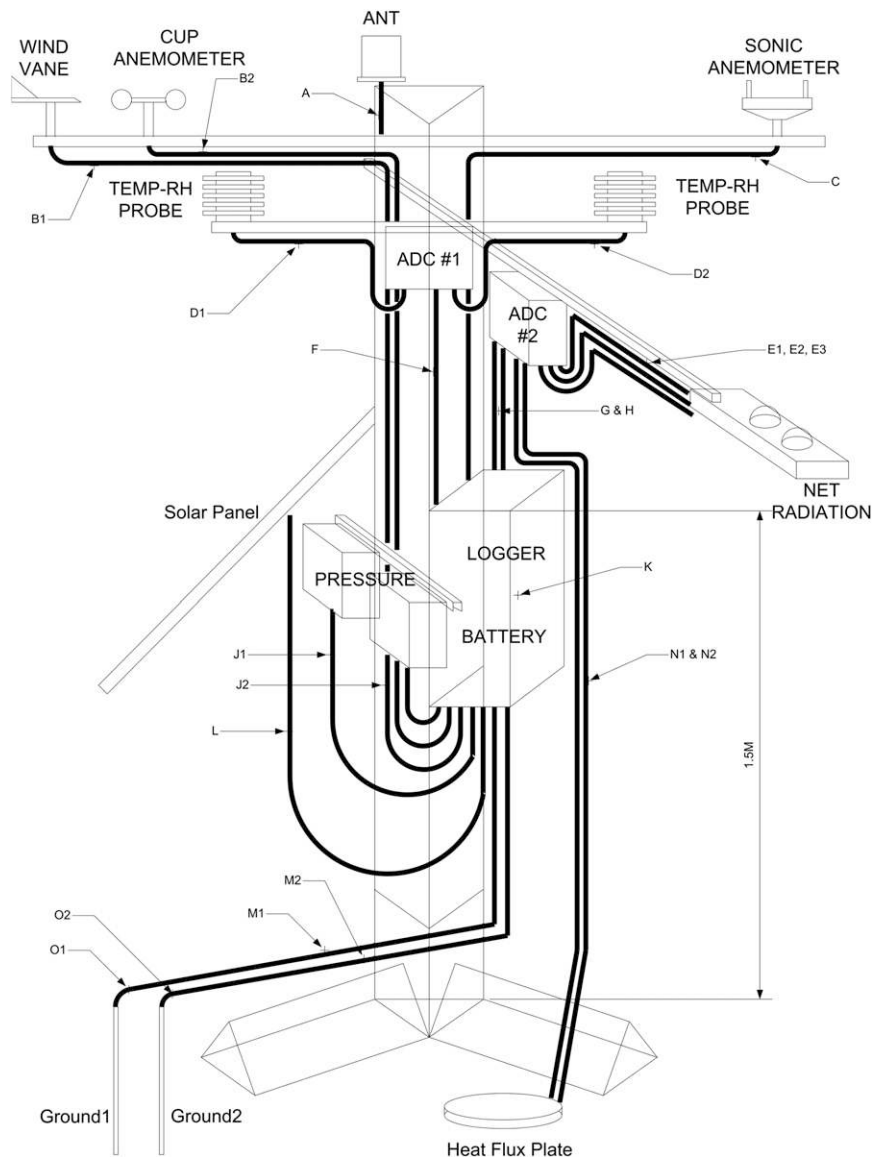
FIG. 1. AWS mechanical structure detailing sensor position on the mast. Mast height is 2.4 m, with each leg (not shown) extend from the base by 2 m. Wind and radiation sensors are mounted on booms extending ~1 m from the mast (see Table 1 for heights).

integrated into the AWS, the design of which is described in section 3.

3. AWS design

The Fennec AWS is shown in Fig. 1 and with a photograph in Fig. 2. The list of observations is summarized in Table 1. Because of the remote AWS locations and the risk of instrument damage or failure in the harsh conditions, redundancy in all measurements has been provided, with the exception of the radiometer owing to cost constraints. Some measurements are duplicated

using alternative technologies, to provide systematic redundancy.

Each AWS is powered from a sealed lead acid battery, which is charged using a solar panel. Despite the Sahara offering significant solar energy, a key goal was to minimize overall power consumption so as to minimize the size and weight of the solar panel and battery, thus easing logistics for desert installation and reducing the risk of components overheating.

The Fennec AWS uses a custom built datalogger. Despite a number of excellent commercial dataloggers being available, it was desirable for autonomy and reliability to

FIG. 2. ONM Algerie staff downloading data from one of the AWSs at sunset. The photograph is taken at a remote location, typical of most of the stations, deep within the Sahara.

construct a system that would consume less power. By maintaining design control over system circuitry, self-heating effects caused by high-current electronics or over specified microprocessors could be minimized. Individual low-level components could be selected to operate under extended temperature conditions—up to +85°C. Furthermore, through careful software design, dependence

on high-level abstract protocols would be unnecessary, minimizing complexity and potential sources of failure.

The basic Fennec logger implements a real-time operating system with power control for a range of peripherals. This basic unit consumes ~60 mW. The details of operation are outside the scope of this paper but are expected to be made available under the GNU General Public License in the future. The logger communicates with the satellite modem using RS232. Additionally, the logger can be interrogated by an external personal computer (PC) over RS232, so as to download any data locally.

The majority of instruments communicate using a dedicated RS485 bus or RS422 line. The bus drivers for each instrument increase overall power consumption to ~180 mW. RS485\RS422 was chosen since it is a balanced communications standard, not requiring a solid reference (e.g., earth), and is relatively noise immune. An RS485-enabled high-precision analog-to-digital converter (ADC) module was designed for analog sensors, which could be mounted as close to the sensor as possible. By converting from an analog voltage to a digital signal close to the source, temperature-induced inaccuracies and noise are kept to a minimum.

Although it would have been possible to operate all sensors from the same RS485 bus, it was considered that this placed overreliance on single components and negated the benefit of using sensor redundancy. However, a single RS485 bus was used for multiple instruments during the calibration procedures. All circuitry was protected from static discharge by selecting RS485 driver components with static protection and using metal oxide

TABLE 1. AWS quantities to be measured.

Measurement	Sensor	Accuracy	Interface	Height (m)
Sonic anemometer (2D wind speed and direction)	Vaisala WMT52	0.3 m s^{-1} 3 °	RS485	2
Cup anemometer (wind speed)	Mierij Meteo MW36	0.5 m s^{-1}	RS422	2
Vane anemometer (wind direction)	Mierij Meteo MW35	3 °	RS422	2
Temperature 1	Epluse EE08	±0.3°C (at 50°C)	V(DC)	2
Humidity 1	Epluse EE08	±2% (at < 90%)	V(DC)	2
Temperature 2	Epluse EE08	±0.3°C (at 50°C)	V(DC)	2
Humidity 2	Epluse EE08	±2% (at < 90%)	V(DC)	2
Thermistor temperature 1	Omega 44007	±0.2°C	V(DC)	2
Thermistor temperature 2	Omega 44007	±0.2°C	V(DC)	2
Pressure 1	Intersema MS5534	±0.5 hPa	Proprietary digital	1
Pressure 2	Intersema MS5534	±0.5 hPa	Proprietary digital	1
Soil temperature	Omega 44007	±0.2°C	V(DC)	−0.1
Soil temperature	Omega 44007	±0.2°C	V(DC)	−0.4
SW radiation upwelling	Kipp & Zonen CNR4	15 W m^{-2}	V(DC)	2
SW radiation downwelling	Kipp & Zonen CNR4	15 W m^{-2}	V(DC)	2
LW radiation upwelling	Kipp & Zonen CNR4	10%	V(DC)	2
LW radiation downwelling	Kipp & Zonen CNR4	10%	V(DC)	2
Ground heat flux	Hukseflux HFP01SC		V(DC)	−0.1
Battery voltage	—	0.1 V	V(DC)	—

varistors (which provide a direct route to ground, if an overvoltage is detected) on all power lines.

The Fennec AWS mechanical structure uses a lightweight aluminum three-chord truss, to produce a 2-m mast with instruments attached by lightweight C-clamps. Since anchoring the AWS using ground anchors would not be possible in sand, a base of three evenly spaced 2-m spars was designed, attached by steel guys to a point halfway up the vertical truss section. Bottle screws are used to tension the guys. Each spar is weighed down with a sand bag, although the wide base provided by the spars makes it very difficult for the AWS to tip. During nearly 6 months of operation and observing a number of haboobs, there is no evidence of an AWS falling over.

Over time a buildup and erosion of sand around the spars is expected at some sites. A solution for this could not be found and would be expected to lead to biases in radiation and wind measurements. Return visits to AWS sites and examination of differences between AWSs over time should allow this effect to be evaluated.

4. Sensor selection

The measurements and sensors used in each AWS are summarized in Table 1, alongside manufacturers' stated accuracy. The stated accuracy does not take into account the effects of signal conditioning electronics, mechanical mounting, and ADC inaccuracies. These sources of error are discussed in section 6.

a. Temperature and relative humidity

The Epluse Elektronik EE08 relative humidity sensors are based on a capacitive element with a dielectric that responds to environmental humidity. A Pt100 temperature sensor is collocated within 2 mm. Signal conditioning and temperature compensation are applied inside the sensor probe, producing an analog voltage. The sensor was chosen for its low cost and limited power consumption while still providing a good level of accuracy. In addition to the Pt100 inside the EE08 sensor, an OMEGA TH-44007 thermistor was used with signal conditioning provided by the AWS precision ADC electronics, thus increasing redundancy and reliance on the EE08 probe. The precision ADC is polled every 200 s.

The EE08 and thermistor probes were mounted in a passive screen. With the high insolation, it would have been preferential to use an aspirated screen. However, an aspirated screen operating under dusty conditions would most likely cause early failure due to mechanical moving parts. This would result in no airflow and poorer measurement than a passive screen. Various solutions involving passive screens with an active pump for low wind speed conditions were considered, but the added complexity requires a larger fan and conflicts with the requirement to minimize power consumption.

b. Wind

Wind measurements are taken using two different forms of sensing technology: a traditional cup anemometer–wind vane combination and a sonic anemometer.

Both sensors have different potential sources of failure. The cup anemometer–wind vane combination has moving parts that will wear excessively in high dust concentration, whereas sonic retrievals can be subject to distortion or complete failure under high dust concentrations.

The Mierij Meteo MW35 cup anemometer and MW36 wind vane were used since they have sealed bearings, which should limit dust ingress and extend life. Both MW35 and MW36 continuously stream data over RS422 with approximately 125 samples being collected every minute.

The sonic anemometer uses "time of flight" theory for a given ultrasonic pulse between transducers to measure airflow in the direction of the signal path. A number of signal paths are used to ascertain a wind vector. The Vaisala WMT52 sonic anemometer was chosen because of its extremely low power consumption of 36 mW. The WMT52 uses three transducers that "bounce" signals off a reflective base plate to other transducers.

c. Radiation

The Kipp & Zonen CNR4 integrates a pyranometer pair, measuring up- and downwelling shortwave (SW) radiation, with a pyrgeometer pair, measuring up- and downwelling longwave (LW) radiation. The pyranometer has a field of view up to nearly 180°, providing global radiation information. A thermistor is embedded within the pyrgeometer to measure its own temperature and therefore correct the longwave measurements.

Radiometers are usually operated from a manned compound, where they are cleaned on a daily basis. Because of the remote locations of the Fennec AWS, this has not been possible. The CNR4 was chosen because of its integrated centrifugal fan. The fan is provided to blow air across the radiometer domes and to minimize the possibility of dust and dew (although considered unlikely in the Sahara) settling and distorting the measurement. Over time, it is fully expected that the lens will become scratched and degraded. However, this should be observed as a slowly increasing measurement bias and relative changes will still be observable. Furthermore, there are two manned flux towers at the periphery of the network (sites 1 and 2 in Fig. 6) with identical radiometers that are cleaned daily. The relative changes across the network in comparison to the flux tower data will enable the AWS degradation to be monitored.

The radiometer fan will eventually fill with dust and wear out. However, the expected time to failure is greater due to the use of a centrifugal fan, where particles are pushed to the outside of the unit. The power consumption of the centrifugal fan is significant and quoted by the manufacturers to be 5 W. Before deployment, measurements within the laboratory showed that the fan consumed close to 2.5 W. It is therefore assumed that 5 W is more likely for an older fan that has been contaminated with dust. Despite these levels of power consumption being at least one order of magnitude greater than that of any other AWS component, the fan was considered desirable to obtain the best possible quality of radiation data.

All radiometers and temperature sensors provide an analog voltage that is measured by an ADC within 0.5 m of the sensor. The necessity for minimal analog signal pathlength, so as to minimize interference potential, is enhanced with the radiometer measurements since the voltages provided are small: $\sim 10~\mu$V (1 W m^{-2})$^{-1}$. The ADC is polled every 200 s.

d. Pressure

The Intersema MS5534 was chosen because of its low power consumption and successful application in a number of previous field projects. The sensors integrate a piezoresistive material with the necessary signal conditioning circuitry. It is interrogated over a proprietary "three wire" digital serial interface. The sensor has been integrated with the circuitry necessary for it to communicate over RS485. Although, it is unnecessary to convert the interface to minimize measurement inaccuracies, RS485 is more suited to longer cable runs. The pressure node is polled every 200 s.

The accuracy of MS5534 is quoted by the manufacturer to be within ±1.5 hPa, although this was improved through further calibration (see section 6).

5. Design solutions

This section describes specific challenges where more development time was applied, producing detailed solutions, worthy of note.

a. Wind measurements

Satellite transmission costs limited the time sampling to 200 s; this sampling period misses some turbulent gusts that may be important for dust uplift (e.g., Koch and Renno 2005; Marsham et al. 2009). Therefore, in addition to the mean, information to compute higher-order parameters of the 200-s wind probability density functions were transmitted.

For every sample period, about 400 cup vane and about 200 sonic anemometer measurements are made.

Since arithmetic division is computationally intensive for an 8-bit microcontroller, the sum of all speed measurements is calculated and transmitted along with the number of measurements, to allow the mean to be computed in postprocessing.

The 200-s sample period will not resolve many turbulent processes. Hence, the AWS also reports the sum of the squared wind speed measurements and the sum of the cubed wind speed measurements, allowing calculation of variance and skew parameters. Wind speed (U) probability distribution can be represented by the Weibull function (Stull 2000):

$$p(U) = \int_{U_1}^{U_2} \left(\frac{k}{c}\right) \left(\frac{U}{c}\right)^{k-1} e^{-(U/c)^k} \, dU, \qquad (1)$$

where $k > 0$ and $c > 0$ are referred to as the "shape" and "scale" parameters of the distribution, respectively. The shape and scale parameters can be calculated from the mean (μ) and variance (σ^2) (Lu et al. 2002), defined as

$$k = \left(\frac{\sigma}{\mu}\right)^{-1.086} \qquad (2)$$

$$c = \frac{\mu}{\Gamma\left(1 + \frac{1}{k}\right)}, \qquad (3)$$

where Γ is the gamma function.

A Weibull distribution can be fitted to any period of AWS data (down to 200 s), calculating the scale and shape parameters from the transmitted $\langle U \rangle$ and $\langle U^2 \rangle$, with the error in the scale and shape dependent on the number of samples used. Lun and Lam (2000) analyze 30 years of Hong Kong wind data to ascertain suitable values for shape and scale: in order to test the behavior of the statistical model, these values were used to create a number of randomly generated Weibull-distributed datasets. Each dataset consisted of 3600 points, comparable to a 1-h dataset from an AWS. The mean, variance, and subsequent shape and scale parameters were calculated from the dataset and compared to the true value. The percentage error in the shape and scale parameters is shown in Fig. 3; demonstrating increased error for low values of shape. Subsequent datasets delivered plots with similar overall trends but subtle variations. By increasing the number of points, the variations diminished. However, using more than 3600 samples, at 1-Hz sampling rate, would not necessarily be representative of the surface layer being monitored, which is likely to be changing over hourly time scales.
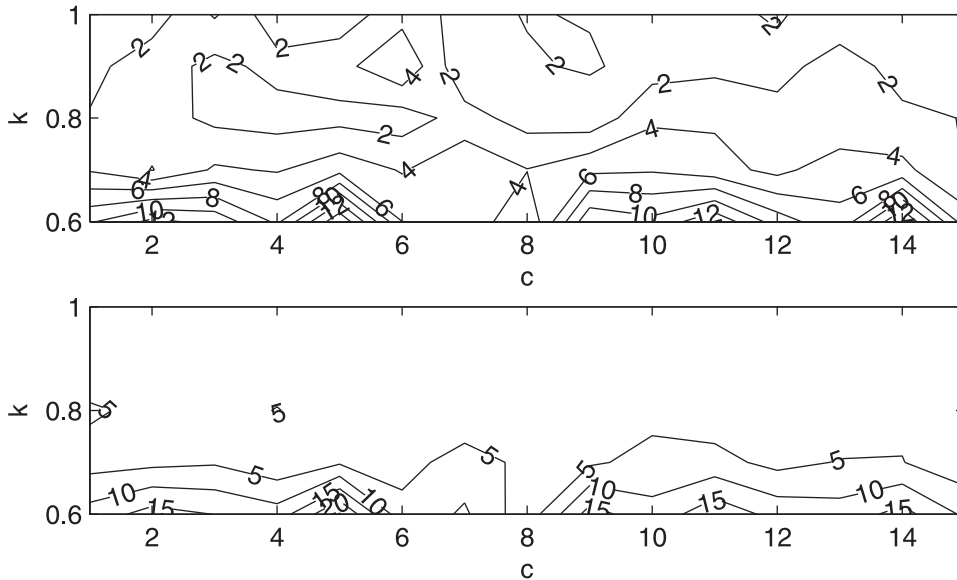
FIG. 3. Percentage error (marked on individual contours) in Weibull shape (k) and scale (c) parameters as calculated from mean and variance of a 3600-sample dataset. Error is shown against the known values of scale and shape for the dataset.

An alternative solution would be to use the skew of the data (calculated from the cubed sum) to further define the distribution, first using high-time-resolution data (20 Hz) from the Fennec supersite at Bordj Bardji Mokhtar (location 1 in Fig. 6) to better test the use of a Weibull probability density function (pdf). Such techniques are the subject of future research. However, section 6a demonstrates the value of simply fitting a Weibull pdf, since this significantly improves the value of the data for studying dust uplift.

b. Data retrieval

Data are transmitted hourly back to the United Kingdom using the Iridium Router-Based Unrestricted Digital Interworking Connectivity Solutions (RUDICS) service, which had been proven effective in Valentic and Stehle (2008), and was more cost effective than the Short Burst Data Service (SBDS) used extensively in other remote instrumentation. The quantity of data required to backhaul precluded the use of European Organisation for the Exploitation of Meteorological Satellites (EUMETSAT) services (EUMETSAT 2011).

RUDICS can be operated in a number of different modes (Iridium Satellite 2004). The Fennec AWS operates in dumb terminal–server mode, which is designed for use with systems without transmission control protocol/Internet protocol (TCP/IP) capability. Given the complexity of developing such protocol capability and subsequent sources of failure, this mode was considered ideal. The dumb terminal, the AWS, initiates a modem

call to a predefined telephone number. The modem used was the Iridium 9522LB, which communicates with the dumb terminal using RS232 serial. Once initiated, a 2400 bits s^{-1} direct "data pipe" is created to a dedicated IP number associated with the predefined number. Data are routed via an Iridium gateway onto the Internet to the dedicated IP address, linked to the data server in the United Kingdom. Multiple connections to the data server are handled simultaneously. However, each AWS is allotted a specific 5-min window every hour to transmit its data. The satellite modem is only powered during this 5-min window. This was implemented to ensure that the modem would not be left powered on indefinitely due to a communications failure, thus leading to a drained battery. In addition, the server could not be overloaded with connections. No quality of service or transmission control is provided by RUDICS. Hence, a specific "handshaking" protocol was developed to maintain robust communication between the remote station and the data server, with minimum bandwidth overhead. The protocol uses a cyclic redundancy check (CRC)-16 checksum calculated over a 222-byte page of data to ensure data integrity. The decision processes required by the remote AWS and the server are shown in Fig. 4. It was found that the Iridium network carried out routine maintenance on a monthly basis, leading to an increase in loss of signal. The handshaking process was therefore necessary to maintain data integrity during such occasions.

Data received in Leeds are subjected to calibration corrections and are subsequently retransmitted to the
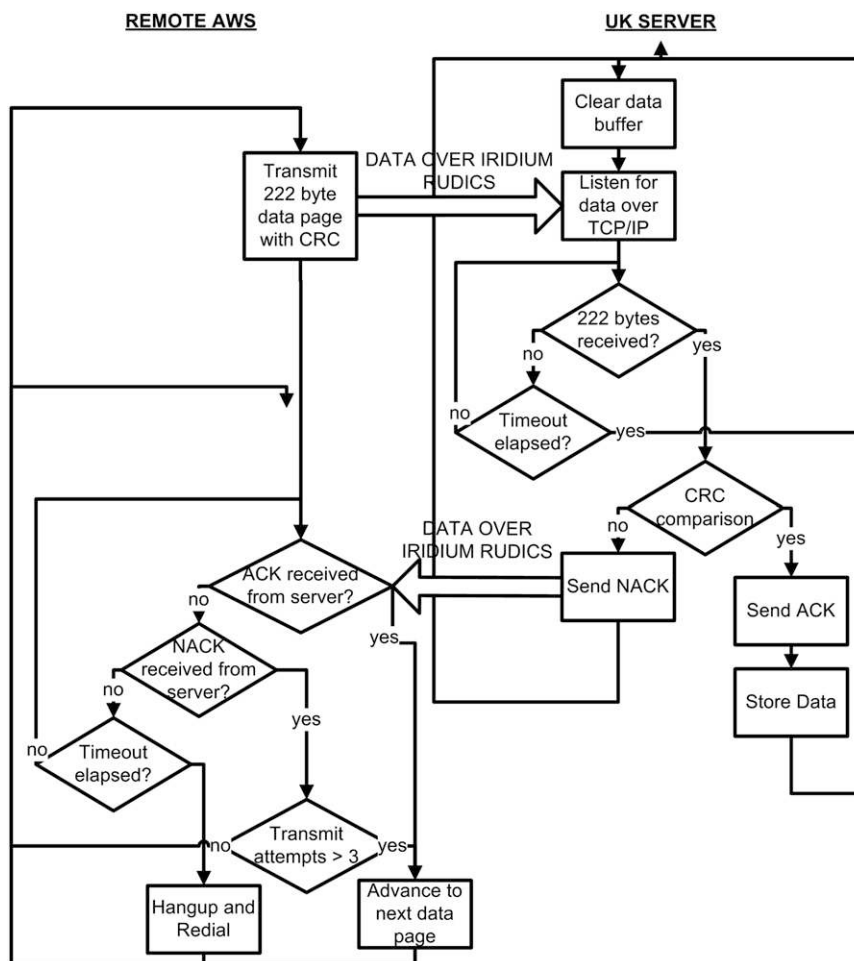
FIG. 4. Handshaking process used to communicate over Iridium RUDICS between remote AWS and server based in Leeds, United Kingdom. (left) Flow diagram describes the decision process within the AWS. (right) Decision process within the Leeds server.

Met Office. Following an initial 2-week testing period, these data are now being used for assimilation and are transmitted onto the meteorological GTS. These data are the first from the remote Sahara to be assimilated by operational weather prediction models in real time.

c. Solar power

Each AWS is powered from a sealed lead acid battery that is charged using a solar panel. It was necessary to keep the solar panel size as small as possible to simplify installation in the remote regions of the Sahara and to reduce wind loading. The model reviewed by Klein (1977) was used for calculating daily radiation values on a tilted plane, taking into account values for the clearness index; K_T was from the peripheries of the Sahara, obtained by Mellit et al. (2008). An angle of 30° was decided upon as a compromise between maximizing solar radiation during the winter and summer months.

The AWS consumes a total of 150 Wh day^{-1}. Ideally, a 40-W panel would have been used, providing enough overhead for dusty panels and inaccuracies in solar modeling. However, market availability of solar panels at 40 W is limited. A Kyocera KC50 solar panel was therefore used with a maximum power output of 54 W and approximate dimensions of 650 mm × 650 mm.

The SEC TLG50 series battery was selected because of its thick plates, which minimize the ageing effects of operation at high temperatures. It is possible that a smaller battery may have been used, but a low-percentage discharge was required to help prolong the battery life under the extreme temperatures in the Sahara.

The charging of the battery was regulated by a Morning Star Sun Guard regulator. The Sun Guard is a series regulator that sits between the solar panel and the battery and minimizes the potential for overcharging the battery by pulse width modulation (PWM) of the solar panel

output once the battery voltage has reached a set point. No load disconnect capability is provided. Previous experience has shown that some "load disconnect" utilities fail to resupply power to the load once charge has increased back to a usable value. The panel has to operate at the battery voltage (plus regulator drop), which will most likely be less than the maximum power point (MPP) voltage (17.4 V), leading to a decrease in overall energy available to the battery. The variation in current below the maximum power point is relatively small. The change in power output is therefore dependent on the ratio of the battery voltage to the MPP voltage.

In many instances, it was found after installation that the energy being consumed was greater than that being produced, resulting in a decreasing battery voltage and failure within several days. This was of particular surprise given the systems were failing during the month of June, under maximum insolation conditions. The data obtained prior to failure demonstrated that the irradiance was in fact greater than had been modeled, implying the overall energy available was greater than expected. A recurring "three peak" pattern was observed in daily battery voltages. The timings of the three peaks across all stations and different days were similar. On days when the radiation data showed significant cloud or dust, the peak magnitudes were smaller. The peak magnitudes grew larger as the initial daily battery voltage dropped, demonstrating less charge in the battery.

It is believed that the solar cell temperature is the cause of this phenomenon. Solar cell efficiency decreases under high temperatures. Although difficult to measure (especially outside laboratory conditions), it is thought that the high insolation coupled with high ambient temperatures, unique to desert regions such as the Sahara, combine to raise the cell temperature. Data from the solar panel datasheet were extrapolated and used to plot the output of the solar panel with increasing cell temperature (Fig. 5). The use of the series regulator will effectively present the battery voltage plus regulator drop (~0.6 V) to the solar panel. Hence, a fully charged battery would represent a ~13.6-V load to the solar panel, for which, from Fig. 5 with a cell temperature of 100°C, the solar panel current output would tend toward 1.7 A—half of that at lower temperatures and originally planned for. This would clearly lead to a decrease in battery voltage over time. The solar panel cell temperature was modeled using irradiation and temperature values recorded by the AWS prior to failure and estimated to be 102.5°C. It is therefore plausible that cell temperature could have become high enough to cause power supply problems.

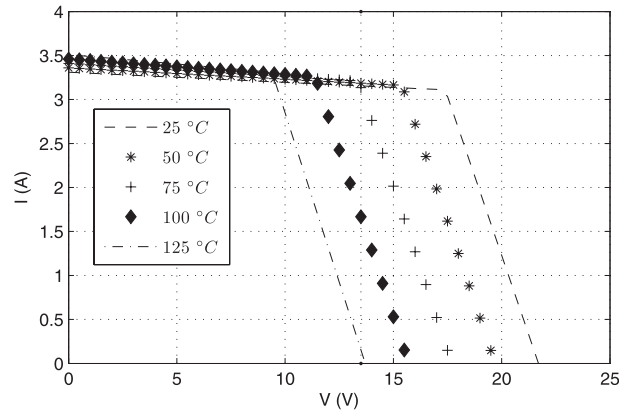To resolve this problem, the solar regulator was changed from the series regulator to a maximum power

FIG. 5. Change in solar panel output with increasing cell temperature. The decrease in solar panel output current with increasing cell temperature for a fixed voltage close to 13.5 V (marked by dotted vertical line) is evident.

point tracker (MPPT) regulator. The MPPT regulator is designed to track the "knee" of the solar panel IV curve (in Fig. 5) irrespective of the load applied. This knee is associated with maximum power output from the solar panel. Such MPPT regulators have increased self-consumption (nearly 20 times that of the series regulator initially installed) with increased complexity. To further minimize the risk of batteries discharging, the radiometer fans were also disconnected, from November 2011 onward.

The proposed solution was tested over a 2-week period in Tamanrasset (22.785°N, 5.522°E), which is at an altitude of ~1000 m and close to the Hoggar Mountains. This means that it is cloudier and cooler than the central Sahara and the insolation of the deep desert rarely occurs. However, the logistics and cost of carrying out the test in the deep desert meant that this was the best that could be achieved. The MPPT regulator performed well under occasional days of high insolation in Tamanrasset, with either flat or increasing battery voltages, demonstrating a net energy surplus. MPPT regulator upgrades were deployed throughout the rest of the network during November 2011.

6. Data quality

Laboratory calibrations were carried out by applying a linear fit between sets of AWS measurements and measurements from a traceable calibrated source. Combined uncertainty of the measurements made and of that of the calibrated source itself was calculated, in keeping with recommendations outlined in JCGM (2008). All laboratory tests were carried out as close as possible to National Institute of Standards and Technology (NIST) standard

TABLE 2. Table of typical expected uncertainties (taken for AWS station 141, shown here for indication only).

				Uncertainty ($k = 1$)				
Humidity (%)				*20*		*50*		*80*
	Epluse 1 (%)			0.61		0.5		0.63
	Epluse 2 (%)			0.61		0.5		0.62
Temperature °C				*5*		*25*		*45*
	Epluse 1 (°C)			0.02		0.03		0.06
	Epluse 2 (°C)			0.05		0.04		0.07
	Thermistor 1 (°C)			0.02		0.02		0.03
	Thermistor 2 (°C)			0.02		0.02		0.02
	Ground temperature 1 (°C)			0.07		0.08		0.15
	Ground temperature 2 (°C)			0.1		0.12		0.2
SW radiation (W m^{-2})				*0*		*200*		*400*
	Upwelling (W m^{-2})			0.6		7		14
				0		*500*		*1000*
	Downwelling (W m^{-2})			0.08		18		35
LW radiation (W m^{-2})		*−700*	*−390*	*−220*	*−140*	*−90*	*0*	*90*	*140*
	Upwelling (W m^{-2})	37.4	20.8	11.8	7.9	5.6	2.6	5.3	7.4
	Downwelling (W m^{-2})	37.4	21.3	12.5	8.2	5.9	6.35	7.7	8.44
Pressure (hPa)				*800–1050 hPa*				
	Sensor 1 (hPa)			0.14				
	Sensor 2 (hPa)			0.15				

laboratory conditions (20°C, 1013.25 hPa). Laboratory calibrations were made around a series of nominal levels. Table 2 includes the uncertainties at these nominal levels for a single AWS, indicating the typical uncertainties. The following section details the calibration methods and provides a brief discussion as to expected sources of error in the field.

a. Humidity

E+E Elektronik EE08 sensors were placed in a Michell Instruments S503 humidity generator, with a Michell Instruments DM509-T-03 used as the standard for comparison. Approximately 100 data points were simultaneously collected asynchronously from the DM509-T-03 and the AWS at each calibration level. It should be noted that the humidity calibration was carried out "end to end" using the same dedicated ADC module as would be used in the field. This ensured a full characterization of all elements in the system that cause uncertainty.

The Epluse Elektronik sensors are mounted in a sun shield naturally ventilated by the wind. During low wind conditions, it is possible for the air to "stagnate" and become overly warmed by the sun. This is discussed further in section 6b.

One of the Fennec AWSs has been collocated with a WMO-manned observation site at Tamanrasset, in Algeria (WMO station 60680). A comparison between the WMO observations and those of the Fennec AWS will enable further assessment of long-term drift in all corresponding measurements.

b. Temperature

The Pt100, embedded inside the EE08 sensor, and the OMEGA TH-44007 thermistor sensors were calibrated using a Fluke 7340 calibration bath with a Fluke 5608 platinum resistance thermometer as the standard resistance measurements of the Fluke 5608 were taken by a Hameg HM 8112 precision voltmeter and the AWS logged the temperature sensor data. As with the humidity, calibration the temperature measurement was calibrated end to end using the same ADC to be used in the field.

Under modest levels of insolation (300–500 W m^{-2}), measurements of temperature using passively ventilated screens demonstrate errors up to 1°C for wind speed conditions less than 1 m s^{-1} (Hubbard et al. 2004). The stronger insolation in the Sahara is likely to cause significantly greater errors at low wind speeds. Further study into this error and methods of correction, given wind speed and radiation measurements, would be of great value. The thermistor embedded in the pyrgeometer is unscreened and may give some indication of likely error for the screened temperature under low wind speed conditions.

c. Pressure

Each pressure module (sensor and supporting RS485-integrated electronics) was connected on a single RS485 bus and addressed using software and a specific node identification number. Calibration was performed using a large vacuum chamber [highly instrumented reactor for atmospheric chemistry (HIRAC) facility, Leeds; Glowacki et al. 2007] with a Paroscientific 745–16B precision barometer.

In the field, pressure inlets to the sensor nodes point down and are subject to being filled with sand and dust over time.

d. Wind

Both sonic and cup–vane anemometers were not calibrated, since they are both sold with individual calibration certificates by the manufacturer demonstrating accuracy to within ± 0.1 m s^{-1}. The sample volumes of the cup–vane and sonic anemometers are designed to be placed at the same height. However, it should be noted that the anemometer mounting bracket is aligned along the east–west axis. Airflow from either of these directions may distort the measurement in the downstream sensor.

Cup anemometers are subject to nonlinear effects due to cup inertia. From the field datasets, the stall speed of the cup anemometer is observed to be ~0.7 m s^{-1}, and the cup inertia can be seen in the comparison between the two datasets. The sonic anemometer is therefore considered to be more responsive to the turbulent gusts.

e. Pyranometer

The Kipp & Zonen CNR4 is individually calibrated by the manufacturer and specific sensitivities are given in μV W^{-1} m^2. The uncertainty in the manufacturer's calibration is 3.5%. Further laboratory tests were intended to characterize the ADC and signal conditioning circuitry.

A 12-V halogen lamp was used as a radiation source, with the distance from the pyranometer used to adjust the irradiation. The pyranometer output was measured using the Hameg HM 8112 precision voltmeter and converted to an irradiance using the manufacturer's sensitivity data. Postcalibration field measurements were observed to increase up to ~1100 W m^{-2} during June 2011. The proportional uncertainty provided by the manufacturer could lead to an uncertainty close to 50 W m^{-2} at these extreme values.

f. Pyrgeometer

As with the pyranometer, the laboratory tests of the pyrgeometer were intended to characterize the ADC

and signal conditioning circuitry across the range of expected field measurements. Creating blackbody sources in the laboratory over the full range was not possible. Therefore, data points across the expected range were simulated as raw voltages applied to the signal conditioning circuitry.

Raw voltages were created using 9-V PP3 batteries at full charge, with low-noise op amp circuitry used to decrease the voltage to the desired levels (covering approximately -700 to $+100$ W m^{-2}). The Hameg precision voltmeter was used to measure the voltages, which were converted to irradiances using the pyrgeometer sensitivity ($\pm 5.6\%$ from the manufacturer). Once again, the proportional uncertainty will continue to increase the uncertainty outside the limits of the calibration.

Accurate measurements of both radiation and wind require the AWS to remain close to vertical. Since the AWS stations are erected on sandy surfaces within the desert, this is difficult to maintain over longer time periods, as sand is scoured and deposited by the wind. A number of stations were visited during November 2011, and no subsidence or tilt was observed over the 6-month installation period.

7. Initial results

a. Saharan boundary layer features

The AWSs were deployed in the Sahara by the Algerian and Mauritanian Offices National de la Météorologie, in May 2011 (map in Fig. 6). The locations and elevations are shown in Table 3. Further missions to renovate systems have been carried out in November 2011. A range of meteorological features can be observed in the data received, and Fig. 7 is discussed as an example (using data from station 34 in Fig. 6). The interpretations of these features are supported by the existing literature and additional measurements from a 15-m flux tower, radiosondes, sodar and lidar instrumentation at site 1 in Fig. 6, and described in Marsham et al. (2013). An in-depth analysis is outside the scope of this paper, and the discussion below is provided so as to provide context to the measurements of the AWS network.

Figure 7 shows data taken from 0600 UTC 17 June to 1000 UTC 18 June 2011. Spinning Enhanced Visible and Infrared Imager (SEVIRI) imagery from Meteosat shows that the AWS site was cloud free throughout this period. In this region it is known that the onset of boundary layer convection after sunrise regularly mixes momentum from nocturnal low-level jets (LLJs) to the surface (e.g., May 1995; Washington et al. 2006; Engelstaedter and Washington 2007; Knippertz 2008; Marsham et al. 2013). The sun rises at around 0600 UTC and the wind
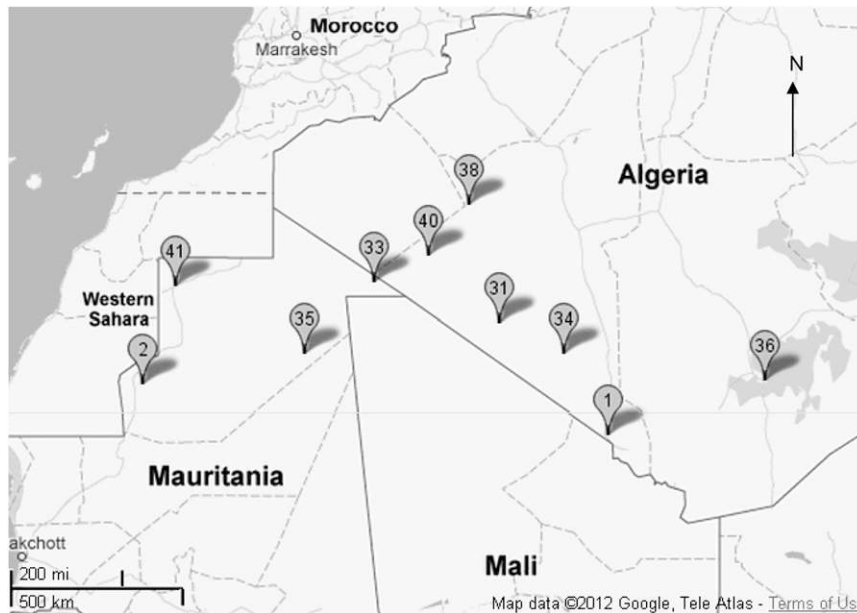
FIG. 6. Map of AWSs installed throughout the Sahara Desert. Each pin represents an AWS and its respective identification number. Note that stations 1 and 2 are not AWS, but manned supersites with identical radiometers to that of the AWSs.

speed maximum between 0700 and 1200 UTC 17 June, with winds exceeding 8 m s^{-1} between approximately 0700 and 1000 UTC, is consistent with this mechanism (this interpretation is supported by forecasts from the Met Office Unified Model, which show a northeasterly jet; not shown). There is a similar but weaker maximum on 18 June, and Birch et al. (2012) show that the flow around the Hoggar Mountains enhances the northeasterly jet in this area. The sun rise at around 0600 UTC, heats the surface, and the deepening boundary layer allows momentum from the nocturnal LLJ to be mixed downward to the surface (e.g., May 1995; Engelstaedter and Washington 2007; Knippertz 2008; Washington et al. 2006). This leads to a wind speed maximum between 0700 and 1200 UTC 17 June, with winds exceeding 8 m s^{-1} between approximately 0700 and 1000 UTC (there is a similar but weaker maximum on 18 June). Wind speeds between 1200 and sunset, at around 1800 UTC, are lower but more variable, consistent with the effects of turbulence from dry boundary layer convection, which also leads to temperature fluctuations up to 2°C (most notably at 1345 and 1530 UTC). After sunset these temperature fluctuations vanish and wind speeds are light in the cooling nocturnal stable layer. There is a sudden warming and wind speed increase at 2100 UTC that lasts until approximately 2230 UTC and a sudden warming, pressure increase, and wind speed increase at 0230 UTC. SEVIRI satellite imagery shows these two events correspond to dust fronts from outflows from a mesoscale convective system to the southeast. The second event represents the arrival of the cold-pool outflow, with the warming and pressure increase consistent with the cold pool being warmer than the near-surface air in the stable boundary layer, but warmer than the air above (Knippertz et al. 2007). The absence of a pressure signal in the first event and the satellite imagery suggest that it is probably a wave excited by the approaching cold pool interacting with the stable nocturnal boundary layer (e.g., Marsham et al. 2011b; if it were simply

TABLE 3. Location and elevation of AWS. Elevation data have been found with respect to mean sea level (MSL; m) using Shuttle Radar Topography Mission (SRTM) data, with an absolute error of <10 m to a 90% confidence level, as shown in Rodriguez et al. (2005, p. 80). Additionally, approximately 1 h of GPS pseudorange and L1 phase data were collected at each site. Further analysis of these data is required find the station elevation with less absolute error.

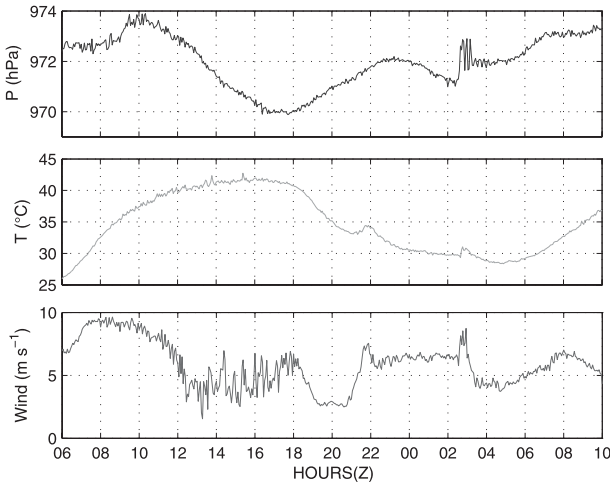| Station No.	Lat	Lon	Elev (SRTM)
31	24.28°N	2.136°W	259
33	25.37°N	5.79°W	336
34	23.503°N	0.299°W	324
35	23.48°N	7.84°W	315
36 (manned site)	22.78°N	5.52°E	1378
41	25.23°N	11.58°W	366
38	27.368°N	3.018°W	375
40	26.053°N	4.221°W	379
01 (manned site)	21.373°N	0.929°E	398
02 (manned site)	22.68°N	12.47°W	590

FIG. 7. Example data from AWS134, located at 23.5°N, 0.4°W: (top to bottom) pressure, temperature, and wind speed from 17 to 18 Jun 2011. Key features of Saharan boundary-layer dynamic meteorology are depicted: mixing of LLJ momentum to the surface (0700–1200 UTC on both days), a cold pool (haboob) at 0230 UTC, and a wave–bore at approximately 2100–2230 UTC.

FIG. 8. Pdfs for wind speed created using mean values for shape (k) and scale (c) calculated for 0600 and 1500 UTC from 6-month AWS data. The variation between 0600 and 1500 UTC demonstrates the variability in the wind with increased turbulence–gustiness in the afternoon.

a shallower cold pool, then it would be expected to move slower than the second cold pool, which is not seen in the Seviri imagery).

b. Use of transmitted wind statistics for studying dust-generating winds

Dust uplift is usually parameterized as a threshold cubic function of friction velocity U^*. This nonlinearity increases the importance of the high wind speed tail of the wind pdf. Using the widely used parameterization of Marticorena and Bergametti (1995), upward dust flux is proportional to horizontal flux, G, with

$$G = \left(\frac{\rho}{g}\right) U^{*3} \left(1 + \frac{U_t^*}{U^*}\right) \left(1 - \frac{U_t^{*2}}{U^{*2}}\right), \qquad (4)$$

where ρ and g are air density and gravitational field constant, respectively; and U_t is the threshold wind speed for uplift, typically found to be ~9 m s^{-1} at 10 m in the Sahara. (Chomette et al. 1999)

Mean pdfs, calculated from Weibull pdfs fitted to transmitted wind statistics (section 5) for all data from May to November from one station are shown in Fig. 8 for 0600 and 1500 UTC. Figure 8 demonstrates the variability in the wind pdf throughout the day, with increased turbulence–gustiness during the afternoon, leading to the half-width of the pdf being over 4 times greater at 1500 compared with 0600 UTC. This change in wind variance through the day demonstrates the value of transmitting, rather than assuming, second- and third-order moments
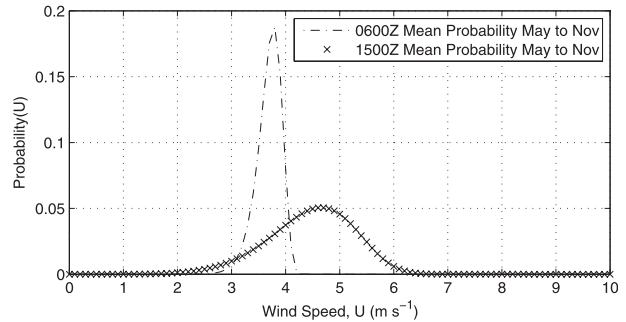
of the wind pdf. Simply using the mean wind to calculate uplift will lead to an underestimation at 1500 as compared with 0600 UTC, due to the greater variance in the afternoon. Furthermore, use of the mean diminishes the effects of sub-200-s turbulent fluctuations, which may contribute to the overall flux estimates.

To investigate the value of transmitting higher-order wind statistics, rather than simply mean wind, for estimating dust uplift, 17 days of 20-Hz sonic anemometer data from a 10-m mast at Bordj Bhadji Mokhtar (BBM) were used, making use of the concept of "uplift potential." Uplift potential, as defined by Marsham et al. (2011a), removes the constant ρ/g term from Eq. (4) and replaces U^* with the near-surface wind speed, U; U^* cannot be directly calculated from the AWS data, but uplift potential defined in this way provides a first-order control on parameterized dust uplift for fixed surface characteristics and controls parameterized dust uplift for a fixed surface under neutral near-surface atmospheric stability, since U^* is then proportional to U.

Uplift potential was calculated from the 20-Hz BBM data in three ways, all using a U_t of 9 m s^{-1}:

(i) "true uplift potential," calculated using the 20-Hz data (smoothed to 1 Hz) and then averaged over 200-s periods;

(ii) "AWS uplift potential," calculated using Weibull distributions of wind speeds, with the Weibull shape and scale parameters calculated from $\langle U \rangle$ and $\langle U^2 \rangle$ from 200-s periods of 20-Hz data smoothed to 1 Hz, that is, simulating the transmitted AWS data; and

(iii) "mean wind uplift potential," calculated from 200-s mean winds.

Figure 9 shows the absolute and percentage errors in the AWS and mean wind uplift potentials when compared to the true uplift potentials. Using each method, the absolute errors increase with increasing wind speed,
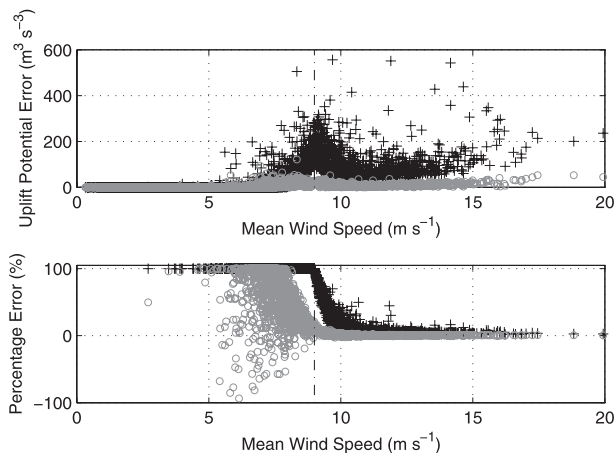
FIG. 9. Error in dust uplift potential calculated using AWS uplift potential (gray circles) and mean wind uplift potential (black plus signs). (top) Absolute error and (bottom) percentage error against mean wind both plotted against mean 200-s wind speed. Positive error is an underestimate of true uplift potential.

but with larger errors when the mean wind is close to the threshold wind speed. Using $\langle U^2 \rangle$ (the AWS uplift potential) greatly reduces the errors, since it represents the nonlinear impact of the high wind speed end of the wind speed pdf, with the mean absolute error approximately 6 times smaller than the uplift potential from the mean wind. Percentage errors in the mean wind uplift potential are small for high mean winds, but they increase rapidly as the mean wind approaches U_t, reaching 100% for mean winds less than U_t, when all uplift potential from the tail of the pdf that exceeds the threshold is missed. These errors are greatly reduced by using the AWS uplift potential, which gives errors less than 10% for mean winds greater than U_t and much less biased random errors for mean winds less than U_t, with significant scatter due to imperfect fits between the Weibull pdfs and the corresponding sets of two hundred 1-s data points.

The variation in the wind speed pdf through the day (Fig. 8) shows that the uplift potential from mean wind cannot simply be tuned to fit the true uplift potential, and the results demonstrate the caution that should be applied to estimating dust uplift from 10-min mean winds reported from surface synoptic (SYNOP) stations, or time step mean winds of this duration from models. Such winds will underestimate uplift in light but gusty winds and miss uplift from dust devils (see also Cakmur et al. 2004; Marsham et al. 2008a). For the 17 days of 20-Hz data analyzed, mean winds less than Ut (9 m s^{-1}) accounted for 4.5% of total uplift potential. Winds less than $U_t + 2$ (11 m s^{-1}) account for approximately 29% of total uplift potential. These features are missed, or greatly underestimated, without using $\langle U^2 \rangle$, leading to an erroneous measure of uplift potential.

8. Summary

The Fennec AWS network measures a range of meteorological parameters, important to further understanding of the Saharan climate. Four stations have been continuously transmitting 200-s data in near–real time (1-h lag), and the temperature data from these stations have been successfully assimilated into forecast models by the Met Office.

A further four stations transmitted data for approximately 1 week to 10 days during late May–early June 2011 before failing because of a lack of power caused by diminished solar panel output under high temperatures and insolation (section 5). These stations have had new regulators installed during November 2011 to overcome this problem. Data have been transmitted from these stations since November 2011, thus enhancing the geographic spread of measurements made.

The data recorded by the Fennec AWS network are of high initial quality due to the time taken to calibrate individual sensors and signal conditioning electronics. This data quality will degrade over time due to the extreme environment in which the stations are located.

The initial data show the value of the AWSs for observing the Saharan heat low, cold-pool outflows from moist convection, boundary layer turbulence and convection, and downward mixing of momentum from the nocturnal low-level jet to the surface. The timing of the LLJ around 0900 UTC is missed by any station reporting at the standard 6-hourly synoptic intervals, and the short-duration high winds from haboobs could be almost completely missed using hourly data.

The AWSs use a novel approach, transmitting the first three moments of the 1-s wind pdf within each 200-s period. This paper has demonstrated that the use of the second moment of the pdf allows significantly better estimates of the dust-generating effects of any 200-s mean wind, especially for mean winds close to the threshold wind speed for dust emission. Results show that dust uplift from 200-s mean winds cannot simply be tuned to account for wind fluctuations, since these fluctuations are greater in the afternoon than the morning and presumably depend on weather conditions. Future studies will investigate the best way to use the transmitted second and third moments for retrievals of the pdfs of wind speeds and friction velocities.

Data from the Fennec AWS network will be made available for users via the British Atmospheric Data Centre (BADC) in due course.

Carl Broomfield for his assistance in writing some of the engineering documentation. Thanks to Bruce Ingleby, Diana Rock, Colin Parrett, and Jon Turton at the Met Office for establishing the relay of data to the GTS.

REFERENCES

Birch, C. E., D. J. Parker, J. H. Marsham, and G. M. Devine, 2012: The effect of orography and surface albedo on stratification in the summertime Saharan boundary layer: Dynamics and implications for dust transport. *J. Geophys. Res.,* **117,** D05105, doi:10.1029/2011JD015965.

Cakmur, R. V., R. L. Miller, and O. Torres, 2004: Incorporating the effect of small-scale circulations upon dust emission in an atmospheric general circulation model. *J. Geophys. Res.,* **109,** D07201, doi:10.1029/2003JD004067.

Chomette, O., M. Legrand, and B. Marticorena, 1999: Determination of the wind speed threshold for the emission of desert dust using satellite remote sensing in the thermal infrared. *J. Geophys. Res.,* **104** (D24), 31 207–31 215.

Cuesta, J., E., and Coauthors, 2008: Multiplatform observations of the seasonal evolution of the Saharan atmospheric boundary layer in Tamanrasset, Algeria, in the framework of the African Monsoon Multidisciplinary Analysis field campaign conducted in 2006. *J. Geophys. Res.,* **113,** D00C07, doi:10.1029/2007JD009417.

Engelstaedter, S., and R. Washington, 2007: Atmospheric controls on the annual cycle of North African dust. *J. Geophys. Res.,* **112,** D03103, doi:10.1029/2006JD007195.

EUMETSAT, 2011: TD16—MeteoSat data collection and distribution service. EUMETSAT Issue v1G, 53 pp.

Flamant, C., J. P. Chaboureau, D. J. Parker, C. A. Taylor, J. P. Cammas, O. Bock, F. Timouk and J. Pelon, 2007: Airborne observations of the impact of a convective system on the planetary boundary layer thermodynamics and aerosol distribution in the inter-tropical discontinuity region of the West African Monsoon. *Quart. J. Roy. Meteor. Soc.,* **133,** 1175–1189, doi:10.1002/qj.97.

Glowacki, D. R., and Coauthors, 2007: Design of and initial results from a highly instrumented reactor for atmospheric chemistry (HIRAC). *Atmos. Chem. Phys.,* **7,** 5371–5390.

Haywood, J. M., and Coauthors, 2011: Motivation, rationale and key results from the GERBILS Saharan dust measurement campaign. *Quart. J. Roy. Meteor. Soc.,* **137,** 1106–1116.

Hubbard, K. G., X. Lin, C. B. Baker, and B. Sun, 2004: Air temperature comparison between the MMTS and the USCRN temperature systems. *J. Atmos. Oceanic Technol.,* **21,** 1590–1597.

Iridium Satellite, L. L. C., 2004: Iridium RUDICS description and VAR interface guide–Release 1.0. Iridium Satellite, 36 pp.

JCGM, 2008: Evaluation of measurement data—Guide to the expression of uncertainty in measurement. JCGM 100:2008, GUM 1995 with minor corrections, 120 pp.

Klein, S. A., 1977: Calculation of monthly average insolation on tilted surfaces. *Sol. Energy,* **19,** 325–329.

Knippertz, P., 2008: Dust emissions in the West African heat trough—The role of the diurnal cycle and of extratropical disturbances. *Meteor. Z.,* **17,** 553–563.

——, C. Deutscher, K. Kandler, T. Müller, O. Schulz, and L. Schütz, 2007: Dust mobilization due to density currents in the Atlas region: Observations from the Saharan Mineral Dust Experiment 2006 field campaign. *J. Geophys. Res.,* **112,** D21109, doi:10.1029/2007JD008774.

Koch, J., and N. O. Renno, 2005: The role of convective plumes and vortices on the global aerosol budget. *Geophys. Res. Lett.,* **32,** L18806, doi:10.1029/2005GL023420.

Lavaysse, C., C. Flamant, S. Janicot, D. J. Parker, J.-P. Lafore, B. Sultan, and J. Pelon, 2009: Seasonal evolution of the West African heat low: A climatological perspective. *Climate Dyn.,* **33,** 313–330.

Lu, L., H. Yang, and J. Burnett, 2002: Investigation on wind power potential on Hong Kong islands—An analysis of wind power and wind turbine characteristics. *Renewable Energy,* **27,** 1–12.

Lun, I. Y. F., and J. C. Lam, 2000: A study of Weibull parameters using long-term wind observations. *Renewable Energy,* **20,** 145–153.

Marsham, J. H., D. J. Parker, C. M. Grams, B. T. Johnson, W. M. F. Grey, and A. N. Ross, 2008a: Observations of mesoscale and boundary-layer scale circulations affecting dust transport and uplift over the Sahara. *Atmos. Chem. Phys.,* **8,** 6979–6993.

——, ——, ——, C. M. Taylor, and J. M. Haywood, 2008b: Uplift of Saharan dust south of the intertropical discontinuity. *J. Geophys. Res.,* **113,** D21102, doi:10.1029/2008JD009844.

——, C. M. Grams, and B. Muhr, 2009: Photographs of dust uplift from small-scale atmospheric features. *Weather,* **64,** 180–181.

——, P. Knippertz, N. S. Dixon, D. J. Parker, and G. M. S. Lister, 2011a: The importance of the representation of deep convection for modeled dust-generating winds over West Africa during summer. *Geophys. Res. Lett.,* **38,** L16803, doi:10.1029/2011GL048368.

——, S. B. Trier, T. M. Weckwerth, and J. W. Wilson, 2011b: Observations of elevated convection initiation leading to a surface-based squall line during 13 June IHOP_2002. *Mon. Wea. Rev.,* **139,** 247–271.

——, and Coauthors, 2013: Meteorology and dust in the central Sahara: Observations from Fennec supersite-1 during the June 1 2011 Intensive Observation Period. *J. Geophys. Res.,* in press.

Marticorena, B., and G. Bergametti, 1995: Modelling the atmospheric dust cycle. 1. Design of a soil-derived dust emission scheme. *J. Geophys. Res.,* **100** (D8), 16 415–16 430.

May, P. T., 1995: The Australian nocturnal jet and diurnal variations of boundary-layer winds over Mt. Isa in north-eastern Australia. *Quart. J. Roy. Meteor. Soc.,* **121,** 987–1003.

Mellit, A., S. A. Kalogirou, S. Shaari, H. Salhi, and A. Hadj Arab, 2008: Methodology for predicting sequences of mean monthly clearness index and daily solar radiation data in remote areas: Application for sizing a stand-alone PV system. *Renewable Energy,* **33,** 1570–1590.

Messager, C., D. J. Parker, O. Reitebuch, A. Agusti-Panareda, C. M. Taylor, and J. Cuesta, 2010: Structure and dynamics of the Saharan atmospheric boundary layer during the West African monsoon onset: Observations and analyses from the research flights of 14 and 17 July 2006. *Quart. J. Roy. Meteor. Soc.,* **136,** 107–124, doi:10.1002/qj.469.

Parker, D. J., C. D. Thorncroft, R. R. Burton, and A. Diongue-Niang, 2005a: Analysis of the African easterly jet, using aircraft observations from the JET2000 experiment. *Quart. J. Roy. Meteor. Soc.,* **131,** 1461–1482.

——, and Coauthors, 2005b: The diurnal cycle of the West African monsoon circulation. *Quart. J. Roy. Meteor. Soc.,* **131,** 2839–2860.

Peyrille, P., and J.-P. Lafore, 2007: An idealized two-dimensional framework to study the West African monsoon. Part II: Large-scale advection and the diurnal cycle. *J. Atmos. Sci.,* **64,** 2783–2803.

Prospero, J., P. Ginoux, O. Torres, S. E. Nicholson, T. E. Gill, 2002: Environmental characterization of global sources of atmospheric soil dust identified with the Nimbus 7 Total Ozone Mapping Spectrometer (TOMS) absorbing aerosol product. *Rev. Geophys.,* **40,** 1002, doi:10.1029/2000RG000095.

Rodriguez, E., C. S. Morris, J. E. Belz, E. C. Chapin, J. M. Martin, W. Daffer, and S. Hensley, 2005: An assessment of the SRTM topographic products. JPL Tech. Rep. JPL D-31639, 143 pp.

Rodwell, M. J., and T. Jung, 2008: Understanding the local and global impacts of model physics changes: An aerosol example. *Quart. J. Roy. Meteor. Soc.,* **134,** 1479–1497.

Stull, R. B., 2000: *Meteorology for Scientists and Engineers.* 2nd ed. Brooks/Cole, 528 pp.

Sultan, B., and S. Janicot, 2003: The West African monsoon dynamics. Part II: The ''preonset'' and ''onset'' of the summer monsoon. *J. Climate,* **16,** 3407–3427.

——, ——, and D. Arona, 2003: The West African monsoon dynamics. Part I: Documentation of intraseasonal variability. *J. Climate,* **16,** 3389–3406.

Valentic, T., and R. Stehle, 2008: First applications of DoD Iridium RUDICS in the NSF polar programs. *Eos, Trans. Amer. Geophys. Union,* **89** (Fall Meeting Suppl.), Abstract IN22A-08.

Washington R., M. Todd, N. J. Middleton, A. S. Goudie, 2003: Dust-storm source areas determined by the total ozone monitoring spectrometer and surface observations. *Ann. Assoc. Amer. Geogr.,* **93,** 297–313.

——, M. C. Todd, S. Engelstaedter, S. Mbainayel, and F. Mitchell, 2006: Dust and the low-level circulation over the Bodélé Depression, Chad: Observations from BoDEx 2005. *J. Geophys. Res.,* **111,** D03201, doi:10.1029/2005JD006502.

WMO, 2008: Measurement of surface wind. *WMO Guide to Meteorological Instruments and Methods of Observation,* 7th ed., WMO-8, I.5-1–I.5-13.